

FAUST I. The hot corino at the heart of the prototypical Class I protostar L1551 IRS5

E. Bianchi,^{1★} C. J. Chandler,² C. Ceccarelli,¹ C. Codella,^{3,1} N. Sakai,⁴ A. López-Sepulcre,^{1,5} L. T. Maud,⁶ G. Moellenbrock,² B. Svoboda,² Y. Watanabe,⁷ T. Sakai,⁸ F. Ménard,¹ Y. Aikawa,⁹ F. Alves,¹⁰ N. Balucani,¹¹ M. Bouvier,¹ P. Caselli,¹² E. Caux,¹³ S. Charnley,¹⁴ S. Choudhury,¹⁰ M. De Simone,¹ F. Dulieu,¹⁵ A. Durán,¹⁶ L. Evans,^{13,3} C. Favre,¹ D. Fedele,³ S. Feng,^{17,18,19} F. Fontani,³ L. Francis,^{20,21} T. Hama,^{22,23} T. Hanawa,²⁴ E. Herbst,²⁵ T. Hirota,¹⁸ M. Imai,²⁶ A. Isella,²⁷ I. Jiménez-Serra,²⁸ D. Johnstone,^{20,21} C. Kahane,¹ B. Lefloch,¹ L. Loinard,^{16,29} M.J. Maureira,¹⁰ S. Mercimek,^{3,30} A. Miotello,⁶ S. Mori,⁹ R. Nakatani,⁴ H. Nomura,³¹ Y. Oba,³³ S. Ohashi,⁴ Y. Okoda,²⁶ J. Ospina-Zamudio,¹ Y. Oya,²⁶ J. Pineda,¹⁰ L. Podio,³ A. Rimola,³³ D. Segura Cox,¹² Y. Shirley,³⁴ V. Taquet,³ L. Testi,⁶ C. Vastel,¹³ S. Viti,³⁵ N. Watanabe,³² A. Witzel,¹ C. Xue,²⁵ Y. Zhang,⁴ B. Zhao,¹⁰ and S. Yamamoto²⁶

¹Univ. Grenoble Alpes, CNRS, IPAG, 38000 Grenoble, France

²National Radio Astronomy Observatory, PO Box O, Socorro, NM 87801, USA

³INAF, Osservatorio Astrofisico di Arcetri, Largo E. Fermi 5, I-50125, Firenze, Italy

⁴RIKEN Cluster for Pioneering Research, 2-1, Hirosawa, Wako-shi, Saitama 351-0198, Japan

⁵Institut de Radioastronomie Millimétrique, 38406 Saint-Martin d'Hères, France

⁶European Southern Observatory, Karl-Schwarzschild Str. 2, 85748 Garching bei München, Germany

⁷Materials Science and Engineering, College of Engineering, Shibaura Institute of Technology, 3-7-5 Toyosu, Koto-ku, Tokyo 135-8548, Japan

⁸Graduate School of Informatics and Engineering, The University of Electro-Communications, Chofu, Tokyo 182-8585, Japan

⁹Department of Astronomy, The University of Tokyo, 7-3-1 Hongo, Bunkyo-ku, Tokyo 113-0033, Japan

¹⁰Max-Planck-Institut für extraterrestrische Physik (MPE), Gießenbachstr. 1, D-85741 Garching, Germany

¹¹Department of Chemistry, Biology, and Biotechnology, The University of Perugia, Via Elce di Sotto 8, 06123 Perugia, Italy

¹²Center for Astrochemical Studies, Max-Planck-Institut für extraterrestrische Physik (MPE), Gießenbachstr. 1, D-85741 Garching, Germany

¹³IRAP, Université de Toulouse, CNRS, CNES, UPS, Toulouse, France

¹⁴Astrochemistry Laboratory, Code 691, NASA Goddard Space Flight Center, 8800 Greenbelt Road, Greenbelt, MD 20771, USA

¹⁵CY Cergy Paris Université, Sorbonne Université, Observatoire de Paris, PSL University, CNRS, LERMA, F-95000, Cergy, France

¹⁶Instituto de Radioastronomía y Astrofísica, Universidad Nacional Autónoma de México, A.P. 3-72 (Xangari), 8701, Morelia, Mexico

¹⁷CAS Key Laboratory of FAST, National Astronomical Observatory of China, Datun Road 20, Chaoyang, Beijing, 100012, P. R. China

¹⁸National Astronomical Observatory of Japan, National Institutes of Natural Sciences, 2-21-1 Osawa, Mitaka, Tokyo 181-8588, Japan

¹⁹Academia Sinica Institute of Astronomy and Astrophysics, No.1, Sec. 4, Roosevelt Rd, Taipei 10617, Taiwan, Republic of China

²⁰Department of Physics and Astronomy, University of Victoria, 3800 Finnerty Road, Elliot Building Victoria, BC, V8P 5C2, Canada

²¹NRC Herzberg Astronomy and Astrophysics 5071 West Saanich Road, Victoria, BC, V9E 2E7, Canada

²²Komaba Institute for Science, The University of Tokyo, 3-8-1 Komaba, Meguro, Tokyo 153-8902, Japan

²³Department of Basic Science, The University of Tokyo, 3-8-1 Komaba, Meguro, Tokyo 153-8902, Japan

²⁴Center for Frontier Science, Chiba University, 1-33 Yayoi-cho, Inage-ku, Chiba 263-8522, Japan

²⁵Department of Chemistry, University of Virginia, McCormick Road, PO Box 400319, Charlottesville, VA 22904, USA

²⁶Department of Physics, The University of Tokyo, 7-3-1, Hongo, Bunkyo-ku, Tokyo 113-0033, Japan

²⁷Department of Physics and Astronomy, Rice University, 6100 Main Street, MS-108, Houston, TX 77005, USA

²⁸Centro de Astrobiología (CSIC-INTA), Ctra. de Torrejón a Ajalvir, km 4, 28850, Torrejón de Ardoz, Spain

²⁹Instituto de Astronomía, Universidad Nacional Autónoma de México, Ciudad Universitaria, A.P. 70-264, Ciudad de México 04510, Mexico

³⁰Università degli Studi di Firenze, Dipartimento di Fisica e Astronomia, via G. Sansone 1, 50019 Sesto Fiorentino, Italy

³¹Division of Science, National Astronomical Observatory of Japan, 2-21-1 Osawa, Mitaka, Tokyo 181-8588, Japan

³²Institute of Low Temperature Science, Hokkaido University, N19W8, Kita-ku, Sapporo, Hokkaido 060-0819, Japan

³³Departament de Química, Universitat Autònoma de Barcelona, 08193 Bellaterra, Spain

³⁴Steward Observatory, 933 N Cherry Ave., Tucson, AZ 85721 USA

³⁵Department of Physics and Astronomy, University College London, Gower Street, London, WC1E 6BT, UK

ABSTRACT

The study of hot corinos in Solar-like protostars has been so far mostly limited to the Class 0 phase, hampering our understanding of their origin and evolution. In addition, recent evidence suggests that planet formation starts already during Class I phase, which, therefore, represents a crucial step in the future planetary system chemical composition. Hence, the study of hot corinos in Class I protostars has become of paramount importance. Here we report the discovery of a hot corino towards the prototypical Class I protostar L1551 IRS5, obtained within the ALMA Large Program FAUST. We detected several lines from methanol and its isotopologues ($^{13}\text{CH}_3\text{OH}$ and CH_2DOH), methyl formate and ethanol. Lines are bright toward the north component of the IRS5 binary system, and a possible second hot corino may be associated with the south component. The methanol lines non-LTE analysis constrains the gas temperature (~ 100 K), density ($\geq 1.5 \times 10^8 \text{ cm}^{-3}$), and emitting size (~ 10 au in radius). All CH_3OH and $^{13}\text{CH}_3\text{OH}$ lines are optically thick, preventing a reliable measure of the deuteration. The methyl formate and ethanol relative abundances are compatible with those measured in Class 0 hot corinos. Thus, based on the present work, little chemical evolution from Class 0 to I hot corinos occurs.

Key words: astrochemistry – ISM: molecules – stars: formation – Individual object: L1551

1 INTRODUCTION

Solar-like planetary systems are the result of a complex process that starts from a cold molecular cloud and evolves through various phases (e.g., Caselli & Ceccarelli 2012). Among them, the Class I protostellar stage, whose typical duration is $\leq 10^5$ yr, represents a crucial link between the youngest Class 0 and the Class II/III protostars (e.g. Crimier et al. 2010), the latter being characterized by developed protoplanetary disks. A recent ALMA breakthrough was the detection of gaps and rings in disks around protostars with ages ≤ 1 Myr (Sheehan & Eisner 2017; Fedele et al. 2018), strongly suggesting that the planet formation process starts already in Class I protostellar disks. Since the process itself and the chemical content of the future planets, asteroids and comets depend on the chemical composition of the disk/envelope, understanding it at the planet-formation scales has become crucial.

However, despite its far reaching importance, the chemical content of Class I protostars is, at the moment, poorly known. Class 0 protostars have infalling-rotating envelopes and circumstellar disks whose chemical composition largely, but not exclusively, depends on the distance from the central accreting object and the composition of the grain mantles (e.g., Caselli & Ceccarelli 2012; Sakai & Yamamoto 2013). Particularly relevant to this Letter, Class 0 protostars possess hot corinos (Ceccarelli 2004), which are defined as warm (≥ 100 K), dense ($\geq 10^7 \text{ cm}^{-3}$) and compact (≤ 100 au) regions enriched in interstellar Complex Organic Molecules (hereinafter iCOMs; Ceccarelli et al. 2017). The chemical composition in these regions is believed to be the result of the sublimation of the grain mantles where the dust reaches about 100 K, regardless of the detailed geometry of the region, whether a spherical infalling envelope or a circumstellar disk. While about a dozen Class 0 hot corinos are imaged so far, only two Class I hot corinos are (De Simone et al. 2017; Bergner et al. 2019a; Belloche et al. 2020). More generally, few studies have focused on Class I protostars, often targeting the envelope or specific molecules (Jørgensen et al. 2004; Codella et al. 2016, 2018; Bianchi et al. 2017, 2019b,a; Bergner et al. 2018, 2019a,b; Artur de la Villarmois et al. 2019a,b; Oya et al. 2019).

The scarcity of available observations makes it difficult to assess whether or not the chemical composition of Class 0 and I protostars differs. Observations of the chemical content of Class I protostars at the planet-formation scale have now become urgent to understand the chemical evolution during the formation of planetary systems around Solar-like stars.

In this context, the ALMA (Atacama Large Millimeter/submillimeter Array) Large Program FAUST (Fifty AU STudy of the chemistry in the disk/envelope system of Solar-like protostars; <http://faust-alma.riken.jp>) is designed to survey the chemical composition of a sample of 13 Class 0/I protostars at the planet-formation scale, probing regions from about 1000 to 50 au (all have a distance ≤ 250 pc). The selected sources represent the protostellar chemical diversity observed at large (≥ 1000 au) scales. All the targets are observed in three frequency setups chosen to study both continuum and line emission from specific molecules: 85.0–89.0 GHz, 97.0–101.0 GHz, 214.0–219.0 GHz, 229.0–234.0 GHz, 242.5–247.5 GHz, and 257.5–262.5 GHz. The FAUST survey provides a uniform sample in terms of frequency setting, angular resolution and sensitivity. We report the first results, obtained towards the prototypical Class I protostar L1551 IRS5. This study focuses on iCOM lines and aims at discovering and studying its hot corino(s).

2 THE L1551 IRS5 SOURCE

L1551 IRS5 is located in Taurus (Strom et al. 1976) at a distance of (141 ± 7) pc (Zucker et al. 2019), has a $L_{\text{bol}} = 30\text{--}40 L_{\odot}$ (Liseau et al. 2005), is a FU Ori-like object (Connelley & Reipurth 2018) and is considered a prototypical Class I source (Adams et al. 1987; Looney et al. 1997). It is surrounded by a large (~ 0.1 pc) rotating/infalling envelope with $A_{\text{v}} > 100$ mag (e.g., Fridlund et al. 2005; White et al. 2006; Moriarty-Schieven et al. 2006) studied via lines from several species such as CH_3OH , HCN, CS, and HCO^+ (e.g., Fridlund et al. 2002; White et al. 2006). L1551 IRS5 is associated with a molecular outflow and the HH154 jet, extensively studied in the X-ray, optical, near IR, and radio emission (e.g., Snell et al. 1980; Fridlund et al. 2005; Schneider et al. 2011, and references therein). Zooming into the inner 100 au, L1551 IRS5 is a binary system, revealed for the first time by VLA cm-observations (Bieging & Cohen 1985) that show two parallel jets

* E-mail: eleonora.bianchi@univ-grenoble-alpes.fr

(Rodríguez et al. 2003b). The binarity was confirmed by BIMA millimeter observations (Looney et al. 1997) that identified a northern source N ($\sim 0.8 M_{\odot}$) and a southern source S ($\sim 0.3 M_{\odot}$) (Liseau et al. 2005). The two protostars are surrounded by a circumbinary disk, whose radius and mass are ~ 140 au and $0.02\text{--}0.03 M_{\odot}$ (Looney et al. 1997; Cruz-Sáenz de Miera et al. 2019). ALMA observations also suggest the presence of two dusty disks ($M_{\text{disk}} > 0.006 M_{\odot}$) towards N and S, with radii between 8 and 14 au. The protostellar disks inclination is expected to be $\sim 35\text{--}45^{\circ}$ for N and $\sim 24\text{--}44^{\circ}$ for S (Cruz-Sáenz de Miera et al. 2019; Lim et al. 2016). Proper motion measurements show an orbital rotation of N and S with a period of ~ 260 yr and an eccentricity orbit tilted by up to 25° from the circumbinary disk (Rodríguez et al. 2003b; Lim et al. 2016).

3 OBSERVATIONS

L1551 IRS5 was observed with ALMA (FAUST Large Program 2018.1.01205.L). The data here exploited were acquired on 2018 October 25 using the C43-5 antenna configuration, with baselines between 15 m and 1.4 km. The analysed spectral window (232.8–234.7 GHz) was observed using spectral channels of 488 kHz (0.63 km s^{-1}). The observations were centered at $\alpha_{J2000} = 04^{\text{h}} 31^{\text{m}} 34^{\text{s}}.14$, $\delta_{J2000} = +18^{\circ} 08' 05''.10$. The quasar J0423-0120 was used as bandpass and flux calibrator, J0510+1800 as phase calibrator. The data were calibrated using the ALMA calibration pipeline within CASA (McMullin et al. 2007) and we included an additional calibration routine to correct for the T_{sys} and spectral data normalization¹. The data were self-calibrated using carefully-determined line-free continuum channels, including corrections for the continuum spectral index, and the continuum model was then subtracted from the visibilities prior to imaging the line data. The resulting continuum-subtracted line-cube, made using a Briggs robust parameter of 0.4, has a synthesized beam of $0''.37 \times 0''.31$ (PA= 39°), and an r.m.s. noise of 1 mJy beam^{-1} in an 0.6 km s^{-1} channel, as expected. We estimate the absolute flux calibration uncertainty of 10% and an additional error of 10% for the spectra baseline determination. Spectral line imaging was performed with the CASA package, while the data analysis was performed using the IRAM-GILDAS package.

4 RESULTS

Figure 1 shows the map towards L1551 IRS5 of the dust emission at 1.3mm and the position of N and S at different dates since 1983. The two objects are not clearly resolved. The deconvolved source size, derived from a 2D Gaussian fit of the emission, is around $0''.4$, similar to the beam size. In addition, it is evident that N is brighter, in agreement with previous observations (Cruz-Sáenz de Miera et al. 2019). The continuum map also shows extended emission ($\sim 1''$ in radius) associated with the circumbinary disk.

Table 1 lists the detected lines from the following iCOMs: methanol and its most abundant isotopologues (CH_3OH , $^{13}\text{CH}_3\text{OH}$, CH_2DOH), methyl formate (HCOOCH_3) and ethanol ($\text{CH}_3\text{CH}_2\text{OH}$). In Fig. 1, we show the integrated intensity (moment 0) maps for one representative line of each molecule. For all lines, the emission peak coincides, within the synthesized beam, with the continuum position peak of source N, although fainter emission

Table 1. Properties of the lines detected towards L1551 IRS5.

Transition	ν^a (GHz)	E_{up}^a (K)	$S\mu^{2a}$ (D^2)	I_{int}^b (K km s^{-1})
$\text{CH}_3\text{OH } 10_{3,7}\text{--}11_{2,9} \text{ E}$	232.9458	190	12	61
$\text{CH}_3\text{OH } 18_{3,15}\text{--}17_{4,14} \text{ A}$	233.7957	447	22	54
$\text{CH}_3\text{OH } 4_{2,3}\text{--}5_{1,4} \text{ A}$	234.6834	61	4	76
$\text{CH}_3\text{OH } 5_{4,2}\text{--}6_{3,3} \text{ E}$	234.6985	123	2	49
$^{13}\text{CH}_3\text{OH } 5_{1,5}\text{--}4_{1,4} \text{ A}$	234.0116	48	4	54
$\text{CH}_2\text{DOH } 3_{3,1} \text{ e}0\text{--}4_{2,2} \text{ e}0$	232.9019	49	0.2	10
$\text{CH}_2\text{DOH } 3_{3,0} \text{ e}0\text{--}4_{2,3} \text{ e}0$	232.9290	49	0.2	34
$\text{CH}_2\text{DOH } 5_{3,2} \text{ o}1\text{--}4_{2,2} \text{ e}0$	233.0831	68	0.2	45
$\text{CH}_2\text{DOH } 5_{3,3} \text{ e}0\text{--}4_{2,3} \text{ o}1$	233.1339	68	0.2	30
$\text{CH}_2\text{DOH } 14_{2,12} \text{ o}1\text{--}14_{1,13} \text{ o}1$	233.1418	261	6	33
$\text{CH}_2\text{DOH } 9_{2,8} \text{ e}1\text{--}9_{1,9} \text{ e}1$	233.4611	123	1.5	34
$\text{CH}_2\text{DOH } 8_{2,6} \text{ e}0\text{--}8_{1,7} \text{ e}0$	234.4710	94	10	59
$\text{HCOOCH}_3 19_{4,16}\text{--}18_{4,15} \text{ A}$	233.2268	123	48	37
$\text{HCOOCH}_3 19_{14,6}\text{--}18_{14,5} \text{ E}$	233.4144	242	23	17
$\text{HCOOCH}_3 19_{12,8}\text{--}18_{12,7} \text{ E}$	233.6710	208	30	17
$\text{HCOOCH}_3 18_{4,14}\text{--}17_{4,13} \text{ E}$	233.7540	114	46	47
$\text{HCOOCH}_3 18_{4,14}\text{--}17_{4,13} \text{ A}$	233.7775	114	46	36
$\text{HCOOCH}_3 19_{11,8}\text{--}18_{11,7} \text{ E}$	233.8452	192	34	31
$\text{HCOOCH}_3 19_{11,9}\text{--}18_{11,8} \text{ E}$	233.8672	192	34	22
$\text{HCOOCH}_3 19_{10,10}\text{--}18_{10,9} \text{ E}$	234.1346	178	37	30
$\text{CH}_3\text{CH}_2\text{OH } 14_{5,9}\text{--}14_{4,10}$	232.9285	120	14	36
$\text{CH}_3\text{CH}_2\text{OH } 13_{5,8}\text{--}13_{4,9}$	233.5710	108	13	18
$\text{CH}_3\text{CH}_2\text{OH } 13_{5,9}\text{--}13_{4,10}$	233.9511	108	13	25
$\text{CH}_3\text{CH}_2\text{OH } 12_{5,8}\text{--}12_{4,9}$	234.2552	97	12	24
$\text{CH}_3\text{CH}_2\text{OH } 10_{5,5}\text{--}10_{4,6}$	234.6663	78	9	28
$\text{CH}_3\text{CH}_2\text{OH } 10_{5,6}\text{--}10_{4,7}$	234.7146	78	9	18

^a Spectroscopic parameters of CH_3OH and $^{13}\text{CH}_3\text{OH}$ are from Xu & Lovas (1997) and Xu et al. (2008), retrieved from the CDMS database (Müller et al. 2005). Those of CH_2DOH , HCOOCH_3 and *anti*- $\text{CH}_3\text{CH}_2\text{OH}$ are from Pearson et al. (2008, 2012) and Ilyushin et al. (2009), retrieved from the JPL database (Pickett et al. 1998). ^b Integrated intensities (T_{B}) derived at the position P3 (Fig. 1). The associated errors are less than 1 K km s^{-1} .

is also detected towards the southern component. The figure also shows the spectra of the $\text{CH}_3\text{OH } 5_{4,2}\text{--}6_{3,3} \text{ E}$ line, extracted in one pixel from different positions across the region in a direction perpendicular to the jet direction. Note that the spectra of the other iCOM lines have the same behavior. Specifically:

IRS5 N: The methanol emission towards N, marked as P3 in Fig. 1, has a double-peaked profile with a central dip at $+7.5 \text{ km s}^{-1}$. The red- and blue-shifted peaks seem associated with gas to the north (positions P1 and P2) and south (P4 and P5) of N, respectively. This velocity pattern, perpendicularly to the jet axis, could be due to either a rotating inner envelope or a disk. Unfortunately, since the emission is not resolved, it is impossible to discriminate between the two possibilities. The spectra of all detected iCOM lines towards position P3, corresponding to the N continuum peak, are shown in Fig. 2, while their spectral parameters are reported in Tab. 1.

IRS5 S: Similarly to N, the lines are double-peaked towards S, with a central dip at $+4.5 \text{ km s}^{-1}$, namely $\sim 3 \text{ km s}^{-1}$ red-shifted with respect to N. Going south (positions P7 and P8) the red peak disappears and only the blue one remains, suggesting again emission from a rotating inner envelope or a disk, assuming that the red peak is mainly associated with S.

¹ [https://help.almascience.org/index.php?/Knowledgebase/Article/View/419;Moellenbrock et al. \(in preparation\).](https://help.almascience.org/index.php?/Knowledgebase/Article/View/419;Moellenbrock%20et%20al.%20(in%20preparation).)

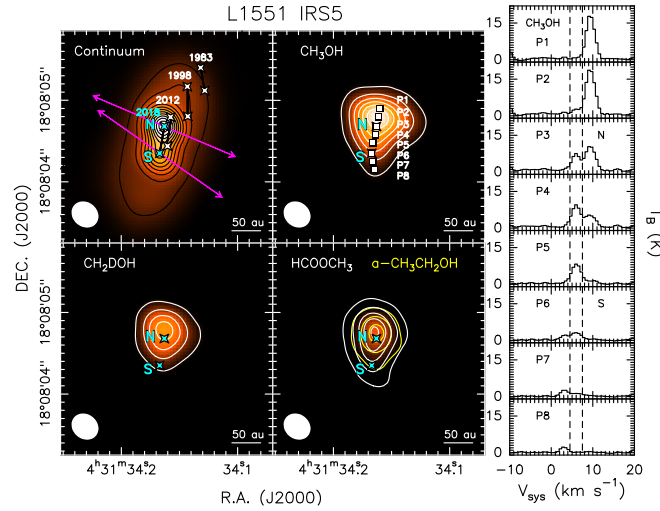


Figure 1. Dust and line emission towards L1551 IRS5. *Left Upper:* 1.3 mm dust continuum emission in colour scale and black contours. First contours and steps are 10σ ($1.8 \text{ mJy beam}^{-1}$) and 100σ , respectively. The white stars indicate the positions of N and S measured in 1983, 1998 and 2012 (Rodríguez et al. 2003a; Lim et al. 2016), while the cyan stars refer to 2018 (this work). The magenta arrows indicate the jet directions (Rodríguez et al. 2003b). *Right Upper:* Colour scale and white contours show the moment 0 map of the $\text{CH}_3\text{OH } 5_{4,2}-6_{3,3}$ E line, integrated over $+2$ to $+15 \text{ km s}^{-1}$. First contours and steps are 8σ ($40 \text{ mJy beam}^{-1} \text{ km}^{-1}$) and 15σ , respectively. The white squares, labelled from P1 to P8, are the different positions where the spectra displayed on the right panels are extracted. The positions P3 and P6 correspond to N and S, respectively. *Left Lower:* Same as for the upper right panel, for the $\text{CH}_2\text{DOH } 8_{2,6}-8_{1,7}$ e0 line, integrated over $+2$ to $+15 \text{ km s}^{-1}$. First contours and steps are 8σ ($42 \text{ mJy beam}^{-1} \text{ km}^{-1}$) and 15σ , respectively. *Right Lower:* Colour scale and yellow contours show the moment 0 map of the $\text{a-CH}_3\text{CH}_2\text{OH } 10_{5,5}-10_{4,6}$ line integrated between $+2$ and $+15 \text{ km s}^{-1}$. First contours and steps are 5σ ($42 \text{ mJy beam}^{-1} \text{ km}^{-1}$) and 10σ , respectively. White contours show the moment 0 map of the $\text{HCOOCH}_3 18_{4,14}-17_{4,13}$ A line integrated between $+2$ and $+12 \text{ km s}^{-1}$. First contours and steps are 5σ ($28.5 \text{ mJy beam}^{-1} \text{ km}^{-1}$) and 10σ , respectively. *Right panel:* $\text{CH}_3\text{OH } 5_{4,2}-6_{3,3}$ spectra extracted at the P1–P8 map positions. The vertical dashed lines mark the systemic velocity inferred towards N ($+7.5 \text{ km s}^{-1}$) and S ($+4.5 \text{ km s}^{-1}$), respectively.

5 COLUMN DENSITIES AND PHYSICAL PARAMETERS

We derived the density and temperature of the gas emitting the methanol lines towards P3 (Tab. 1), along with the molecular abundances of the detected iCOMs. To this end, we carried out a non-LTE analysis of the CH_3OH lines via the Large Velocity Gradient (LVG) code by Ceccarelli et al. (2003). We used the collisional coefficients of $\text{CH}_3\text{OH-A}$ and $\text{CH}_3\text{OH-E}$ with para-H_2 computed between 10 and 200 K for the first 256 levels of each species (Rabli & Flower 2010), provided by the BASECOL database (Dubernet et al. 2013). We assumed a spherical geometry (de Jong et al. 1980), a $\text{CH}_3\text{OH-A/CH}_3\text{OH-E}$ ratio equal to 1, a $^{12}\text{C}/^{13}\text{C}$ ratio equal to 60 (Milam et al. 2005), a line FWHM equal to 3.5 km s^{-1} as measured, and that the levels are populated by collisions and not by the absorption of the dust background photons whose contribution is very likely negligible due to the low values of the CH_3OH Einstein coefficients. We ran a large grid of models ($\geq 10^4$) covering a $\text{CH}_3\text{OH-A}$ ($N_{\text{CH}_3\text{OH-A}}$) and $\text{CH}_3\text{OH-E}$ column density from 3×10^{16} to $4 \times 10^{19} \text{ cm}^{-2}$, an H_2 number density (n_{H_2}) from 3×10^6 to $2 \times 10^8 \text{ cm}^{-3}$, and a gas temperature (T_{kin}) from 80 to 180 K. We found the solution with the lowest χ^2 by simultaneously fitting the $\text{CH}_3\text{OH-A}$, $\text{CH}_3\text{OH-E}$ and $^{13}\text{CH}_3\text{OH-A}$ lines, leaving the $N_{\text{CH}_3\text{OH-A}}$, n_{H_2} , T_{kin} , and the emitting size (the emission is unresolved) as free parameters. Since the collisional coefficients are available for only the three lines with the upper level energy less than 200 K, only those were used. The best fit is obtained with $N_{\text{CH}_3\text{OH-A}} = 1 \times 10^{19} \text{ cm}^{-2}$ and a size of $0''.15$ (21 au). Solutions with $N_{\text{CH}_3\text{OH-A}} \geq 0.5 \times 10^{19} \text{ cm}^{-2}$ are within the 1σ confidence level. All the observed CH_3OH lines are optically thick ($\tau > 50$), as well as the $^{13}\text{CH}_3\text{OH-A}$ ($\tau \sim 2$) one, which makes the size well constrained. The temperature is $(100 \pm 10) \text{ K}$ and the density is $\geq 1.5 \times 10^8 \text{ cm}^{-3}$ at 1σ confidence level. The results do not

change if we assume a line FWHM of 3.0 or 4.0 km s^{-1} and they as the line optical depths are weakly model-dependent because of the $^{13}\text{CH}_3\text{OH}$ line detection.

Collisional rates are not available for the other molecules, so we used the Rotational Diagram analysis to estimate their column densities, assuming a source size of $0''.15$ as derived from the methanol analysis. In the case of CH_2DOH , we derive a rotational temperature of $88 \pm 9 \text{ K}$ and a column density $(64 \pm 11) \times 10^{16} \text{ cm}^{-2}$. However, as the non-LTE methanol line analysis shows that even the $^{13}\text{CH}_3\text{OH}$ line is optically thick, we expect the same for the CH_2DOH lines, so that the derived column density is a lower limit. For HCOOCH_3 and $\text{CH}_3\text{CH}_2\text{OH}$, the E_{up} range covered by the detected lines is not large enough, so we assumed a rotational temperature of 100 K , based on the methanol LVG analysis, to derive the respective column densities. They are $(33 \pm 2) \times 10^{16}$ and $(149 \pm 13) \times 10^{15} \text{ cm}^{-2}$, for methyl formate and ethanol, respectively. With these column densities, the predicted opacity is around 0.3 – 0.5 for the methyl formate lines and ~ 0.2 for the ethanol lines. Therefore, both column densities (Table 2) are not affected by the line opacity.

6 DISCUSSION AND CONCLUSIONS

6.1 The hot corinos of L1551 IRS5

The derived gas temperature and the detection of iCOMs make L1551 IRS5 N a hot corino. The present data also suggest the presence of a second hot corino in S, to be confirmed by higher spatial resolution observations. This increases, and perhaps doubles, the number of known Class I hot corinos as, before this work, only two were imaged, SVS13-A (De Simone et al. 2017; Belloche et al. 2020) and Ser-emb 17 (Bergner et al. 2019a). Besides, our observations are the first to provide the chemical richness

Table 2. List of detected iCOMs towards L1551 IRS5 N.

Species	N_{lines}^a	E_u (K)	T_{rot}^b (K)	N_{tot}^b (cm^{-2})
non-LTE analysis				
CH ₃ OH	3	61–190	100(10)	$\geq 1 \times 10^{19} c$
¹³ CH ₃ OH	1	48		
Rotational Diagram analysis				
CH ₂ DOH	7	49–261	88(9)	$\geq 5 \times 10^{17}$
HCOOCH ₃	8	114–242	100 ^d	$33(2) \times 10^{16} d$
CH ₃ CH ₂ OH	6	78–120	100 ^d	$149(13) \times 10^{15} d$

^a Number of lines used in the analysis. ^b Parameters derived adopting a source size of $0''.15$, as derived by the non-LTE analysis of the methanol lines. Upper limits and error bars (in parenthesis) are at 1σ confidence level. ^c Total methanol column density. ^d To derive the column density we assumed T_{rot} equal to 100 K, as derived by the methanol non-LTE analysis.

of Class I protostars on a Solar System scale. The derived emitting size for N of $0''.15$, equivalent to about 20 au, is consistent with the heating from the central $40 L_{\odot}$ source, and does not necessarily require an outburst activity. However, note that the $0''.15$ sizes are derived assuming a filling factor from a circular gaussian source emission. If the emission is more elongated in one direction, as would be the case in a rotating envelope and/or disk, this could explain the slightly more extended emission of Fig. 1.

One result of the present work is that the methanol lines towards L1551 IRS5 N are very optically thick. This implies that we can only establish a lower limit to the true methanol column density. This large methanol line opacity very likely is not a unique property of L1551 IRS5 and it is even more dramatic in Class 0 protostars, with their larger material column densities with respect to Class I sources. This was already clear from the observations of IRAS16293–2422, where CH₃¹⁸OH was used to derive the methanol column density (Jørgensen et al. 2016). Even more dramatically, recent VLA observations showed extremely optically thick methanol lines towards NGC1333 IRAS4A1 and IRAS4A2 (De Simone et al. 2020). Here we show that even in Class I hot corinos the estimation of the column density of methanol assuming that the ¹³C isotopologue lines are optically thin can be inaccurate. This fact could explain the contradictory results found by Bianchi et al. (2019b) when comparing the iCOM abundances normalised to methanol in different Class 0 and I protostars. A reliable measure requires the ¹⁸O methanol isotopologue detection.

Finally, given the high line optical depths, we can not estimate the methanol deuteration, because both the derived methanol and deuterated methanol column densities are lower limits, $\geq 1 \times 10^{19} cm^{-2}$ and $\geq 5 \times 10^{17} cm^{-2}$, respectively. Taking these at face value, methanol deuteration would be of 5%. Again, to obtain a reliable measure requires the detection of ¹³CH₂DOH.

6.2 Methyl formate and ethanol in Class 0 and I sources

The methyl formate and ethanol abundances relative to methanol are ≤ 0.03 and ≤ 0.015 , respectively (Tab. 2). The methyl formate normalised abundance is compatible with what measured, at comparable spatial scales, towards the Class 0 hot corinos IRAS 16293–2122B (0.03; Jørgensen et al. 2018), HH212 (0.03; Lee et al. 2019), IRAS 4A and IRAS 2A (0.005 and 0.016; Taquet et al. 2015; López-Sepulcre et al. 2017). The ethanol normalised abundance in L1551 IRS5 N is also similar to the normalized abundances measured in the Class 0 hot corinos men-

tioned above, namely 0.006–0.02. Finally, both methyl formate and ethanol normalised abundances are similar to those measured in the Class I hot corino of SVS13-A, 0.016 and 0.014, respectively (Bianchi et al. 2019b). A more reliable comparison can be obtained by considering the abundance ratio between methyl formate and ethanol, which are both optically thin. In L1551 IRS5 N, this value is ~ 2 , a factor 2 larger than that measured in the Class 0 IRAS16293–2122B (Jørgensen et al. 2018) and Class I SVS13-A (Bianchi et al. 2019b). Considering all the uncertainties, the Class I L1551 IRS5, similarly to SVS13-A, does not look dramatically different from Class 0 hot corinos with respect to the iCOM relative abundances.

ACKNOWLEDGEMENTS

This project has received funding from : 1) the European Research Council (ERC) under the European Union’s Horizon 2020 research and innovation program, for the Project “The Dawn of Organic Chemistry” (DOC), grant agreement No 741002; 2) the PRIN-INAF 2016 The Cradle of Life - GENESIS-SKA (General Conditions in Early Planetary Systems for the rise of life with SKA); 3) a Grant-in-Aid from Japan Society for the Promotion of Science (KAKENHI: Nos. 18H05222, 19H05069, 19K14753); 4) the Spanish FEDER under project number ESP2017-86582-C4-1-R; 5) DGAPA, UNAM grants IN112417 and IN112820, and CONACyT, Mexico; 6) ANR of France under contract number ANR-16-CE31-0013; 7) the French National Research Agency in the framework of the Investissements d’Avenir program (ANR-15-IDEX-02), through the funding of the “Origin of Life” project of the Univ. Grenoble-Alpes, 8) the European Union’s Horizon 2020 research and innovation programs under projects “Astro-Chemistry Origins” (ACO), Grant No 811312. This paper makes use of the following ALMA data: ADS/JAO.ALMA#2018.1.01205.L. ALMA is a partnership of ESO (representing its member states), NSF (USA) and NINS (Japan), together with NRC (Canada), MOST and ASIAA (Taiwan), and KASI (Republic of Korea), in cooperation with the Republic of Chile. The Joint ALMA Observatory is operated by ESO, AUI/NRAO and NAOJ. The National Radio Astronomy Observatory is a facility of the National Science Foundation operated under cooperative agreement by Associated Universities, Inc. We thank the referee, Paul Ho, for his insightful suggestions.

DATA AVAILABILITY: The raw data will be available on the ALMA archive at the end of the proprietary period (ADS/JAO.ALMA#2018.1.01205.L).

REFERENCES

- Adams F. C., Lada C. J., Shu F. H., 1987, *ApJ*, **312**, 788
- Artur de la Villarmois E., Jørgensen J. K., Kristensen L. E., Bergin E. A., Harsono D., Sakai N., van Dishoeck E. F., Yamamoto S., 2019a, *A&A*, **626**, A71
- Artur de la Villarmois E., Kristensen L. E., Jørgensen J. K., 2019b, *A&A*, **627**, A37
- Belloche A., et al., 2020, *A&A*, **635**, A198
- Bergner J. B., Guzmán V. G., Öberg K. I., Loomis R. A., Pegues J., 2018, *ApJ*, **857**, 69
- Bergner J. B., Martín-Doménech R., Öberg K. I., Jørgensen J. K., Artur de la Villarmois E., Brinch C., 2019a, *ACS Earth and Space Chemistry*, vol.~3, issue 8, pp.~1564-1575, **3**, 1564
- Bergner J. B., Öberg K. I., Walker S., Guzmán V. V., Rice T. S., Bergin E. A., 2019b, *ApJ*, **884**, L36
- Bianchi E., et al., 2017, *MNRAS*, **467**, 3011
- Bianchi E., Ceccarelli C., Codella C., Enrique-Romero J., Favre C., Lefloch B., 2019a, *ACS Earth and Space Chemistry*, **3**, 2659

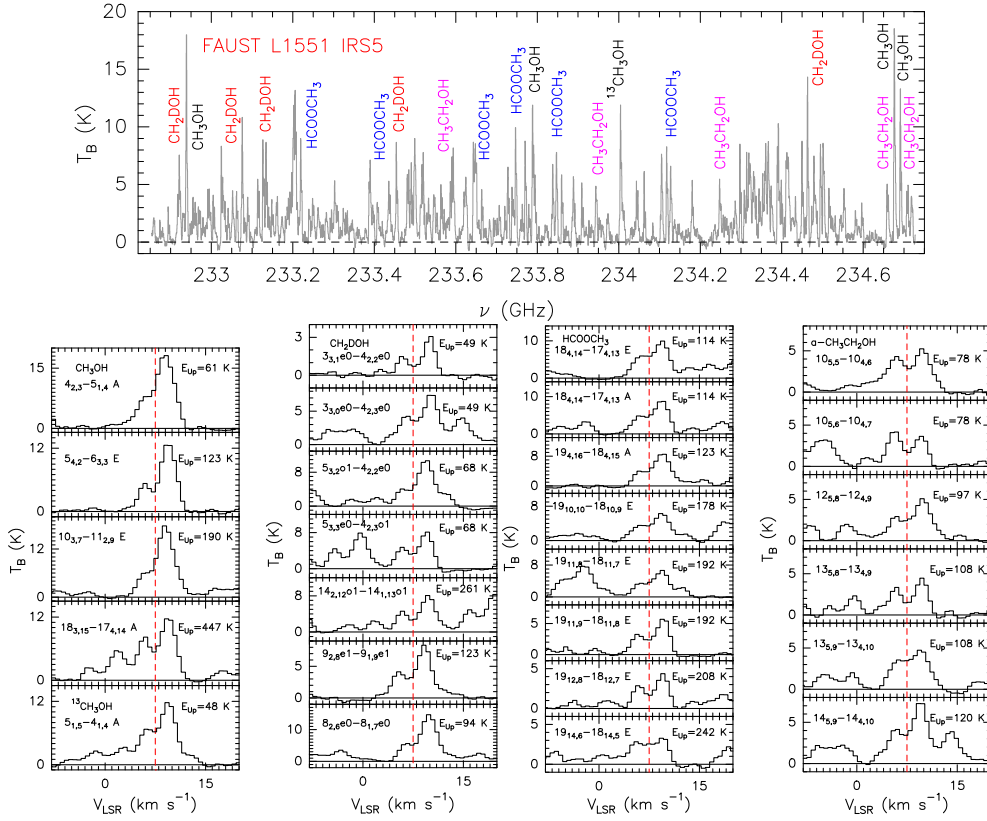


Figure 2. Observed line spectra (in T_B scale) towards IRS5 N (P3 position of Fig. 1). *Upper panel:* Entire spectrum between 232.8 and 234.7 GHz. *Lower panels:* Spectra of CH_3OH , $^{13}\text{CH}_3\text{OH}$, CH_2DOH , HCOOCH_3 and *anti*- $\text{CH}_3\text{CH}_2\text{OH}$: transitions and upper level energies are reported in the upper left and right corner of each panel, respectively. The vertical dashed line marks the ambient LSR velocity ($+7.5 \text{ km s}^{-1}$).

- Bianchi E., et al., 2019b, *MNRAS*, **483**, 1850
 Bieging J. H., Cohen M., 1985, *ApJ*, **289**, L5
 Caselli P., Ceccarelli C., 2012, *A&ARv*, **20**, 56
 Ceccarelli C., 2004, *The Hot Corinos of Solar Type Protostars*. p. 195
 Ceccarelli C., Maret S., Tielens A. G. G. M., Castets A., Caux E., 2003, *A&A*, **410**, 587
 Ceccarelli C., et al., 2017, *ApJ*, **850**, 176
 Codella C., et al., 2016, *A&A*, **586**, L3
 Codella C., et al., 2018, *A&A*, **617**, A10
 Connelley M. S., Reipurth B., 2018, *ApJ*, **861**, 145
 Crimier N., et al., 2010, *A&A*, **516**, A102
 Cruz-Sáenz de Miera F., Kóspál Á., Ábrahám P., Liu H. B., Takami M., 2019, *ApJ*, **882**, L4
 De Simone M., et al., 2017, *A&A*, **599**, A121
 De Simone M., et al., 2020, *ApJ*, **896**, L3
 Dubernet M.-L., et al., 2013, *A&A*, **553**, A50
 Fedele D., et al., 2018, *A&A*, **610**, A24
 Fridlund C. V. M., Bergman P., White G. J., Pilbratt G. L., Tauber J. A., 2002, *A&A*, **382**, 573
 Fridlund C. V. M., Liseau R., Djupvik A. A., Hultgren M., White G. J., Favata F., Giardino G., 2005, *A&A*, **436**, 983
 Ilyushin V., Kryvda A., Alekseev E., 2009, *Journal of Molecular Spectroscopy*, **255**, 32
 Jørgensen J. K., Schöier F. L., van Dishoeck E. F., 2004, *A&A*, **416**, 603
 Jørgensen J. K., et al., 2016, *A&A*, **595**, A117
 Jørgensen J. K., et al., 2018, *A&A*, **620**, A170
 Lee C.-F., et al., 2019, *ApJ*, **879**, 101
 Lim J., Yeung P. K. H., Hanawa T., Takakuwa S., Matsumoto T., Saigo K., 2016, *ApJ*, **826**, 153
 Liseau R., Fridlund C. V. M., Larsson B., 2005, *ApJ*, **619**, 959
 Looney L. W., Mundy L. G., Welch W. J., 1997, *ApJ*, **484**, L157
 López-Sepulcre A., et al., 2017, *A&A*, **606**, A121
 McMullin J. P., Waters B., Schiebel D., Young W., Golap K., 2007, *CASA Architecture and Applications*. p. 127
 Milam S. N., Savage C., Brewster M. A., Ziurys L. M., Wyckoff S., 2005, *ApJ*, **634**, 1126
 Moriarty-Schieven G. H., Johnstone D., Bally J., Jenness T., 2006, *ApJ*, **645**, 357
 Müller H. S. P., Schlöder F., Stutzki J., Winnewisser G., 2005, *Journal of Molecular Structure*, **742**, 215
 Oya Y., et al., 2019, *ApJ*, **881**, 112
 Pearson J. C., Brauer C. S., Drouin B. J., 2008, *Journal of Molecular Spectroscopy*, **251**, 394
 Pearson J. C., Yu S., Drouin B. J., 2012, *Journal of Molecular Spectroscopy*, **280**, 119
 Pickett H. M., Poynter R. L., Cohen E. A., Delitsky M. L., Pearson J. C., Müller H. S. P., 1998, *J. Quant. Spectrosc. Radiative Transfer*, **60**, 883
 Rabli D., Flower D. R., 2010, *MNRAS*, **406**, 95
 Rodríguez L. F., Curiel S., Cantó J., Loinard L., Raga A. C., Torrelles J. M., 2003a, *ApJ*, **583**, 330
 Rodríguez L. F., Porras A., Claussen M. J., Curiel S., Wilner D. J., Ho P. T. P., 2003b, *ApJ*, **586**, L137
 Sakai N., Yamamoto S., 2013, *Chemical Reviews*, **113**, 8981
 Schneider P. C., Günther H. M., Schmitt J. H. M. M., 2011, *A&A*, **530**, A123
 Sheehan P. D., Eisner J. A., 2017, *ApJ*, **851**, 45
 Snell R. L., Loren R. B., Plambeck R. L., 1980, *ApJ*, **239**, L17
 Strom K. M., Strom S. E., Vrba F. J., 1976, *AJ*, **81**, 320
 Taquet V., López-Sepulcre A., Ceccarelli C., Neri R., Kahane C., Charnley S. B., 2015, *ApJ*, **804**, 81
 White G. J., Fridlund C. W. M., Bergman P., Beardsmore A., Liseau R., Price M., Phillips R. R., 2006, *ApJ*, **651**, L41

- Xu L.-H., Lovas F. J., 1997, [Journal of Physical and Chemical Reference Data](#), 26, 17
- Xu L.-H., et al., 2008, [Journal of Molecular Spectroscopy](#), 251, 305
- Zucker C., Speagle J. S., Schlafly E. F., Green G. M., Finkbeiner D. P., Goodman A. A., Alves J., 2019, [ApJ](#), 879, 125
- de Jong T., Boland W., Dalgarno A., 1980, *Astronomy and Astrophysics*, 91, 68

This paper has been typeset from a $\text{\TeX}/\text{\LaTeX}$ file prepared by the author.